Viscosity and surface-tension effects on wave generation by a translating body

R. W. YEUNG* and P. ANANTHAKRISHNAN**
Department of Mechanical Engineering, University of California at Berkeley,
*CA 94720-1740, USA, **Present address: Department of Ocean Engineering, Florida Atlantic University,*
Boca Raton, FL 33431, USA.

Abstract. Various theoretical and experimental studies have been carried out to examine the generation of waves ahead of a translating body. Not all issues pertaining to this wave-motion problem are, however, fully resolved. In particular, mechanisms pertaining to generation of white-water instability and inception of vortices in the bow region are not fully understood. In this paper, the two-dimensional, unsteady, nonlinear, viscous-flow problem associated with a translating surface-piercing body is solved by means of a finite-difference algorithm based on boundary-fitted coordinates. Effects of surface tension and surfactants are examined. Results of this work resolve certain classic issues pertaining to bow flows. A continuous generation of short and steepening bow waves is observed at low (draft) Froude number, a nonlinear phenomenon uncovered recently in the case of inviscid fluid also. This indicates that, steady-state nonlinear bow-flow solution may not exist, even at low speed. It is postulated that these short bow waves are responsible for the white-water instability commonly observed ahead of a full-scale ship. The amplitudes of these short bow waves are suppressed by surface tension, which is, possibly, the reason why white-water instability is not distinctly observed in laboratory-scale experiments. The presence of surfactants on the free surface is found to intensify the generation of free-surface vorticity, thus resulting in the formation of bow vortices. The accumulation of surface-active contaminants at the bow is hence responsible for the generation of bow vortices observed in laboratory experiments at low Froude number. At high Froude number, an impulsive starting motion of the body results in the generation of a jet-like splash at the bow and a gentle start an overturning bow wave, as previously observed in the case of inviscid bow flow.

Key words: surface tension, gravity, viscosity, bow waves, boundary-fitted coordinates, finite differences.

1. Introduction

Motivated by the experimental finding that breaking bow waves could significantly increase a vessel's powering requirement [1], hydrodynamicists have investigated the mechanisms associated with the generation of bow waves. Such studies have revealed some interesting bow-flow phenomena. For example, experimental results of Suzuki [2] and Honji [3] showed that the flow approaching a surface-piercing body separates upstream, thus resulting in the generation of bow vortices. Fitting of a bulb to a blunt bow was found to accelerate the fluid at the bow in such a way that bow vorticity and the wave-breaking component of ship resistance was reduced ([4], [5]). These observations suggested that viscosity could play a key role in the bow-flow problem. Using the *double-body* potential-flow solution and the assumption that surface tension balances the normal component of the viscous stress vector on the free surface, Patel *et al.* [6] obtained a criterion for flow separation ahead of the body. Despite these crude assumptions, experimental results agree with this criterion qualitatively well ([7]). On the other hand, Lugt [8] argued that surface tension should not provide any criterion for flow separation. His analysis, which was based on a local expansion of the governing equations, showed that

---

* Author for correspondence, e-mail: rwyeung@socrates.berkeley.edu

the dividing streamline is normal to the free surface. However, dividing streamlines that are normal to the free surface have not been observed in experiments ([7]).

Mori [9] claimed that short bow-wave breakings, observable as white water at low speed prior to complete bow-wave breakdown, is due to the instability of free-surface shear layer and hence due to turbulence. However, Maruo and Ikehata [10] refuted this claim. Experimental work of Maruo and Ikehata demonstrated that a free-surface shear layer of sufficient strength is generated primarily as a consequence of wave breaking, not because of viscosity effects due to the curviness of the free surface. Their results also suggested that spilling-type bow-wave breaking is substantially suppressed by surface tension at low speed.

Dagan and Tulin [11] considered bow-wave breaking as a local Taylor instability in a potential-flow model. Their second-order solution based on a small draft-Froude number expansion showed that bow-wave breaking could occur when the Froude-number is O(1). Assuming the flow to be steady-state *a priori*, Tuck and Vanden-Broeck [12, 13] extended the above analysis to the fully nonlinear case. They argued that *inviscid* bow- and stern-flow problems are reversible; in other words, a splashless stagnation-type bow-flow solution, if it exists, would correspond to a waveless stern-flow solution. Attempts were then made to construct waveless bow geometries ([14] and [15]).

Nonlinear, unsteady, *inviscid* bow-flow solutions were obtained by Grosenbaugh and Yeung [16] for some general body shapes. Overturning bow waves were observed above a certain critical draft-Froude number, which was found to be dependent on the bow geometry. In particular, it was found that the incorporation of a bulbous profile increases the critical Froude number. Application of the above solution procedure for the low-Froude-number case showed that bow waves of decreasing lengths are continually generated, implying that steady-state nonlinear bow-flow solutions may not exist even at low Froude number [17]. Based on these inviscid-flow results, Yeung [17] conjectured that these short bow waves may be responsible for the white-water instability observed ahead of a full-scale ship operating at low draft-Froude number.

Direct numerical solution of the incompressible Navier–Stokes equations had also been obtained to determine viscosity effects on bow flows. Most of these computations were based on the so-called *marker-and-cell* method, with a drawback that the free-surface boundary conditions can be implemented only approximately. In particular, the presence of surface tension and surfactants, which could play crucial roles at low speed, cannot be easily incorporated into such a method. Nevertheless, using this method, Miyata [18] did obtain some qualitatively accurate results in the high-Froude-number regime.

This brief review clearly indicates that certain fundamental issues pertaining to the bow-flow problem remain unresolved. For example, mechanisms responsible for white-water instability and the origin of bow vorticity at low speed are yet to be fully understood. Recently, in order to resolve these issues, we have solved numerically the two-dimensional nonlinear bow-flow problem including the effects of viscosity, surface tension, and surfactant ([19] and [20]). The analysis and the findings, which resolve some of the classic issues, are presented in this paper.

2. Problem formulation

Referring to Figure 1, we use a fixed (inertial) coordinate system Oxy, with the x-axis along the calm-water level and the y-axis pointing upwards. A two-dimensional surface-piercing body of draft D is assumed to translate in the positive x-direction with velocity U. The domain
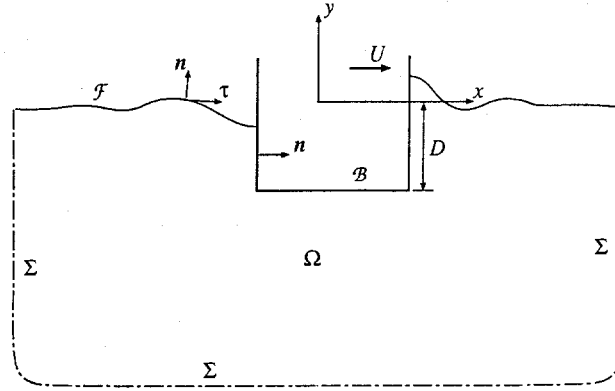
Figure 1. Flow due to a translating two-dimensional body: coordinate system and notations.

of the fluid is denoted by Ω and its boundary by $\partial\Omega$, which consists of the body contour $\mathcal{B}$, free surface $\mathcal{F}$, and a far-field open boundary Σ. Unit, outward normal- and tangential-vectors on $\partial\Omega$ are denoted by $\mathbf{n} = (n_1, n_2)$ and $\boldsymbol{\tau} = (\tau_1, \tau_2)$, respectively. Acceleration of gravity is denoted as g. The fluid, of density ρ, is assumed to be incompressible, homogeneous, and Newtonian. The coefficient of kinematic viscosity of the fluid is denoted by ν and that of the dynamic viscosity μ. All flow variables presented henceforth are nondimensionalized with respect to U, ρ, and D.

2.1. FIELD EQUATIONS

The field equations governing the viscous bow-flow problem are the incompressible Navier–Stokes equations given by:

$$\nabla \cdot \mathbf{u} = 0, \tag{1}$$

$$\frac{\partial \mathbf{u}}{\partial t} + \mathbf{u} \cdot \nabla \mathbf{u} = -\nabla P + \frac{1}{Re}\nabla^2 \mathbf{u} \quad \text{in } \Omega. \tag{2}$$

Here $P = P(\mathbf{x}, t)$ denotes the dynamic pressure

$$P = p + \frac{y}{F_d^2},$$

with $p = p(\mathbf{x}, t)$ being the gage pressure at position $\mathbf{x}$. The unknown quantities are velocity $\mathbf{u}(\mathbf{x}, t) \equiv (u, v)$ and pressure $p(\mathbf{x}, t)$ fields. The parameters Re and F_d, defined by

$$Re \equiv \frac{UD}{\nu} \quad \text{and} \quad F_d \equiv \frac{U}{\sqrt{gD}}$$

are the Reynolds and Froude numbers based on the body draft, respectively.

2.2. FREE-SURFACE BOUNDARY CONDITIONS

Since the free surface $\mathcal{F}$ is a material surface, its temporal evolution is governed by

$$\frac{\mathrm{D}}{\mathrm{D}t}\mathbf{X} = \mathbf{u}, \tag{3}$$

where $\mathbf{X} \equiv (X, Y) \in \mathcal{F}$ and D/Dt denotes the material derivative. Continuity of stress-vector components across a *clean* surface along the normal and tangential directions is given by (*e.g.*, [21]):

$$-p + \frac{2n_1^2}{Re}\frac{\partial u}{\partial x} + \frac{2n_2^2}{Re}\frac{\partial v}{\partial y} + \frac{2n_1n_2}{Re}\left(\frac{\partial u}{\partial y} + \frac{\partial v}{\partial x}\right) = \frac{\kappa}{We} \tag{4}$$

and

$$\frac{2\tau_1 n_1}{Re}\frac{\partial u}{\partial x} + \frac{2\tau_2 n_2}{Re}\frac{\partial v}{\partial y} + \frac{\tau_1 n_2 + \tau_2 n_1}{Re}\left(\frac{\partial u}{\partial y} + \frac{\partial v}{\partial x}\right) = 0 \quad \text{on } \mathcal{F}, \tag{5}$$

where κ denotes the local curvature of the free surface. We denotes the Weber number:

$$We \equiv \frac{\rho U^2 D}{\sigma_c}, \tag{6}$$

where σ_c is the surface-tension coefficient of a *clean* free surface.

The above stress conditions need to be modified to account for the presence of a surfactant, which, depending on its concentration, alters the surface tension and thus induces a gradient in surface tension along $\mathcal{F}$. This surface-tension gradient is balanced by the tangential component of the viscous-stress vector on the free surface [22].

Surfactants can undergo mass diffusion besides being convected by the flow. In this work, we consider only the case of *insoluble* surfactants which, by definition, are transported only along the free surface, but not into the fluid. Conservation of such surfactants on the free surface is governed by the following transport equation:

$$\frac{\partial C}{\partial t} + \frac{\partial}{\partial s}(Cu_\tau) = \frac{1}{R_s}\frac{\partial^2}{\partial s^2}C \quad \text{on } \mathcal{F}, \tag{7}$$

where s denotes an arc-length parameter along $\mathcal{F}$ and u_τ the tangential component of the fluid velocity. The surfactant concentration is denoted by $C = C(s, t)$ and the nondimensional coefficient of surface diffusion by R_s.

Since the surface-tension coefficient σ depends on surfactant concentration, *i.e.* $\sigma = \sigma(C)$, the free-surface stress conditions become

$$-p + \frac{2n_1^2}{Re}\frac{\partial u}{\partial x} + \frac{2n_2^2}{Re}\frac{\partial v}{\partial y} + \frac{2n_1n_2}{Re}\left(\frac{\partial u}{\partial y} + \frac{\partial v}{\partial x}\right) = \frac{\kappa}{We}\frac{\sigma}{\sigma_c} \tag{8}$$

and

$$2\tau_1 n_1\frac{\partial u}{\partial x} + 2\tau_2 n_2\frac{\partial v}{\partial y} + (\tau_1 n_2 + \tau_2 n_1)\left(\frac{\partial u}{\partial y} + \frac{\partial v}{\partial x}\right) = -E\frac{\partial C}{\partial s} \quad \text{on } \mathcal{F}, \tag{9}$$

where the parameter

$$E \equiv \frac{D}{\nu U}\left|\frac{\mathrm{d}\sigma}{\mathrm{d}C}\right| \tag{10}$$

represents the variation of surface tension with respect to surfactant concentration. We call E the *surfactant number;* this is related to the so-called Marangoni number, a terminology commonly used in the literature on physicochemical hydrodynamics for a nondimensional parameter similar to E (*e.g.*, [23]). A general property of surfactants is that dσ/dC is negative;

in other words, surface tension decreases with an increase in surfactant concentration. In order to define E as a positive quantity, we used the modulus of $\mathrm{d}\sigma/\mathrm{d}C$ for the definition of E and appropriately included a negative *sign* on the right-hand side of Equation (9). We also assume that the variation of surface tension with respect to surfactant concentration is linear; thus, we can take E as a constant.

The surfactant concentration C at a given t is determined by integration of the surfactant-transport Equation (7) with respect to time. Note that the transport of surfactants is governed by the fluid flow which in turn, through the free-surface conditions, is governed by the surfactant distribution on $\mathcal{F}$. Hence, both the Navier–Stokes and the surfactant-transport equations have to be solved concurrently.

It has been observed in laboratory experiments that surface-active contaminants accumulate at the bow and affect the flow physics only at very low Froude number. At high Froude number, the contaminants are washed away by flow convection and hence the effect of surfactant is not significant (see [22] and [7]). At very low Froude number, the free-surface deformation is negligible. For the purpose of understanding the effect of surfactants on low-speed bow flows at laboratory scale, it is therefore justifiable to assume that the free surface remains undeformed and flat. The equations corresponding to the presence of surfactant on a flat free surface, which we consider for examining the effect of surfactant on low-Froude-number bow flow, are given by

$$Y = 0, \qquad v = 0, \qquad \frac{\partial u}{\partial y} = -E\frac{\partial C}{\partial x}, \quad \text{and} \tag{11}$$

$$\frac{\partial C}{\partial t} + \frac{\partial}{\partial x}(Cu) = \frac{1}{R_s}\frac{\partial^2 C}{\partial x^2} \quad \text{on } \mathcal{F}. \tag{12}$$

2.3. BODY BOUNDARY CONDITION

Velocity of the fluid particles on the body boundary is determined by the familiar no-slip and no-flux conditions:

$$u = U, \qquad v = 0 \quad \text{on } \mathcal{B}. \tag{13}$$

Modeling the movement of the contact points $\mathcal{B} \cap \mathcal{F}$ is, however, not so trivial. Application of the no-slip condition at $\mathcal{B} \cap \mathcal{F}$ results in a singularity of the fluid stress, which is basically due to the incompatibility of body and free-surface boundary conditions. Numerous investigations (*e.g.*, [24], [25], and [26]) have been carried out in recent years and yet no definitive model has been developed for modeling the movement of the contact point. The molecular-dynamics simulation of Koplik *et al.* [26] shows that fluid indeed slips at the contact line, but its precise form, from the continuum viewpoint, is not clear. However, several approximate conditions have been examined in recent years for modeling the movement of contact points (*e.g.*, [27] and [28]). In the present work, for modeling the movement of the contact points we replace the no-slip condition with *zero* shear-stress (free slip) condition, which is compatible with the adjacent free-surface condition, over a small length on $\mathcal{B}$ at and near $\mathcal{B} \cap \mathcal{F}$: *i.e.*

$$u = U, \qquad \frac{\partial v}{\partial x} = 0 \quad \text{on } \mathcal{B} \text{ at and near } \mathcal{B} \cap \mathcal{F}. \tag{14}$$

This model is based on the *local-slippage* model used by Huh and Mason [28], in which it is assumed that fluid slips freely over a small distance near the contact line. While a sensitivity

analysis of this model is not the focus of the present study, our results demonstrate that it is plausible to simulate the movement of the contact line for a wide range of Froude numbers with this model.

2.4. OTHER CONDITIONS

Finally, for closure, we impose the following approximation on the far-field open boundary Σ:

$$P = 0 \quad \text{on } \Sigma \text{ at all time.} \tag{15}$$

The velocity on Σ is determined by a spatial extrapolation that is consistent with the solution method. Since the above approximate modeling of the open boundary could cause spurious reflections of waves incident on Σ, we position Σ at a sufficiently large distance from the body and also terminate the simulation once the body-generated leading transient wave reaches Σ.

The body motion is started impulsively from a quiescent state, *i.e.* both velocity field and free-surface elevation are set to zero at time $t = 0$.

3. Solution method

The fully nonlinear unsteady free-surface flow problem is solved in primitive variables by means of a fractional-step finite-difference algorithm based on boundary-fitted coordinates. More details of this solution procedure are given in [19, 20, 29]. For completeness, an overview of the solution procedure is given in this section.

3.1. SOLUTION OF FIELD EQUATIONS WITH BOUNDARY CONDITIONS

As per the primitive-variables-based fractional-step method, an intermediate *auxiliary* velocity field $\mathbf{u}^*(\mathbf{x})$ is first computed by use of the momentum Equation (2) without the pressure-gradient term:

$$\mathbf{u}^*(\mathbf{x}) = \mathbf{u}(\mathbf{x}, t_{k-1}) + \delta t \, \mathcal{R}(\mathbf{x}, t_{k-1}), \tag{16}$$

where δt denotes the time-step size and subscript k the instant of discrete time, *e.g.* $t_k = k \, \delta t$. Further, $\mathcal{R}(\mathbf{x}, t_{k-1})$ denotes an explicit differencing of the convection and diffusion terms where we use the known velocity field at t_{k-1}. In the present work, we use first-order upwind differencing for discretizing the *coordinate-transformed* convection term and second-order central differencing for the diffusion term of the momentum equation. We can write the difference scheme for the complete Navier–Stokes equations, following the notations used in Equation (16), as

$$\mathbf{u}(\mathbf{x}, t_k) = -\delta t \, \nabla P(\mathbf{x}, t_k) + [\mathbf{u}(\mathbf{x}, t_{k-1}) + \delta t \, \mathcal{R}(\mathbf{x}, t_{k-1})], \tag{17}$$

where

$$\nabla \cdot \mathbf{u}(\mathbf{x}, t_k) = 0. \tag{18}$$

By comparing Equations (16) and (17), we observe that the auxiliary velocity field $\mathbf{u}^*(\mathbf{x})$ can be expressed as a direct sum of the actual divergence-free velocity $\mathbf{u}(\mathbf{x}, t_k)$ and pressure-gradient $\nabla P(\mathbf{x}, t_k)$ fields: *i.e.*

$$\mathbf{u}^*(\mathbf{x}) = \mathbf{u}(\mathbf{x}, t_k) + \delta t \nabla P(\mathbf{x}, t_k), \quad \text{where } \nabla \cdot \mathbf{u}(\mathbf{x}, t_k) = 0. \tag{19}$$

We decompose the auxiliary velocity field $\mathbf{u}^*(\mathbf{x})$ into $\mathbf{u}(\mathbf{x}, t_k)$ and $\nabla P(\mathbf{x}, t_k)$ fields in a sequential manner. We first determine the pressure field by solving a Poisson equation obtained by taking the divergence of Equation (19):

$$\nabla^2 P(\mathbf{x}, t_k) = \frac{1}{\delta t} \nabla \cdot \mathbf{u}^*(\mathbf{x}). \tag{20}$$

The correctional effect of the pressure is then incorporated into $\mathbf{u}^*(\mathbf{x})$ to evaluate $\mathbf{u}(\mathbf{x}, t_k)$ as

$$\mathbf{u}(\mathbf{x}, t_k) = \mathbf{u}^*(\mathbf{x}) - \delta t \, \nabla P(\mathbf{x}, t_k), \tag{21}$$

which follows from the decomposition relation (19). The above fractional-step procedure is an extension of the *projection* method, developed by Chorin [30, 31] for the solution of the incompressible Navier–Stokes equations, to include the treatment of the presence of a free surface, which is governed by kinematic as well as stress-vector continuity conditions.

The boundary conditions for $\mathbf{u}^*(\mathbf{x})$ on the body contour $\mathcal{B}$ and the free surface $\mathcal{F}$ are obtained from the decomposition relation (Equation 19), (see also [32]). On the open boundary Σ, $\mathbf{u}^*(\mathbf{x})$ is evaluated by spatial extrapolation.

For the solution of the pressure Poisson Equation (20), homogeneous Neumann condition, obtained in a manner consistent with the solution method, is used on $\mathcal{B}$. The normal-stress condition (Equation (4) or (8)) is used to obtain a Dirichlet condition for pressure on $\mathcal{F}$. On Σ, the assumption that the dynamic pressure is zero for all time (Equation (15)) provides homogeneous Dirichlet condition for the pressure Poisson equation.

The velocity on $\mathcal{B}$ is determined by the kinematic condition (Equations (13) and (14)). On Σ, the decomposition (Equation (19)) is completed to evaluate $\mathbf{u}(\mathbf{x}, t_k)$. On $\mathcal{F}$, Neumann-type conditions are obtained for the velocity components by use of the stress conditions. After computing the velocity field in the domain Ω by means of Equation (21), we use these Neumann conditions to determine the velocity components on $\mathcal{F}$. The kinematic condition (3) is integrated to advance the free-surface boundary in time. For better accuracy, a two-step predictor-corrector algorithm is used to implement the free-surface boundary conditions. At each instant of time, the surfactant-conservation equation (see (11)) is solved explicitly to determine the surfactant concentration. First-order upwind differencing is used for the discretization of the convection term and second-order central-differencing for the diffusion term of the surfactant conservation equation.

3.2. BOUNDARY-FITTED COORDINATES

The geometry of the present nonlinear free-surface flow problem is not only arbitrary, but also evolving in time. Even so, we can solve the governing flow equations in a fixed uniform mesh if boundary-fitted coordinates are exploited. The use of curvilinear coordinates further enables us to implement the boundary conditions accurately. In this procedure, the physical space (x, y) is mapped to an uniform computational space (ξ, η) (see Figure 2). The governing
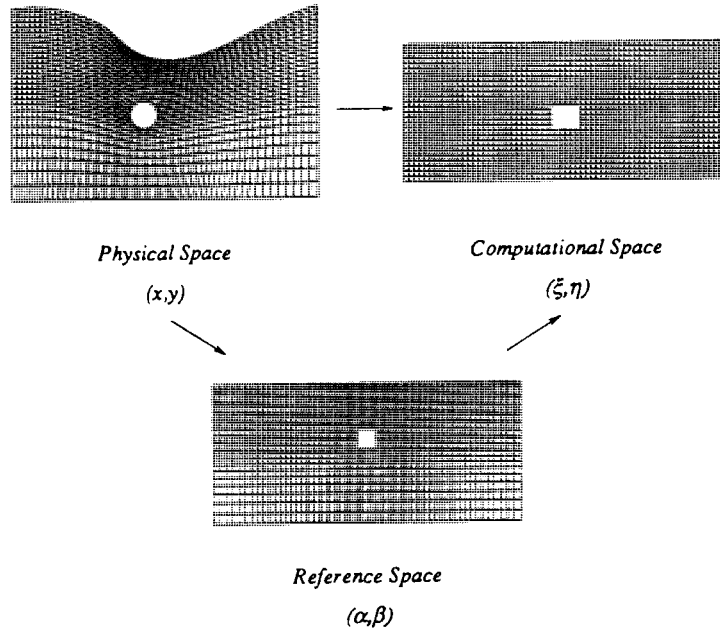
Figure 2. Generation of boundary-fitted coordinates using reference space.

flow equations are also transformed to (ξ, η) space and, thus, the fractional-step algorithm for the solution of the Navier–Stokes equations is implemented in the uniform computational mesh (ξ, η). For the purpose of controlling grid properties such as grid spacings (smoothness), cell-area distribution, and orthogonality, we use the concept of an intermediate reference space (α, β). The grid properties, desired in the physical space (x, y), are first obtained in the reference space (α, β) which is geometrically similar, but simpler than the physical space (see Figure 2). We then transfer the grid-properties of the reference mesh to the physical space (x, y), using a variational formulation [19, 29]. Variational calculus then leads to a set of differential equations for the grid. Depending on the desired properties that we would like to control, different grid equations result. The field equations for the grid functions are presented below with a typographical error in [29, Equations (29–30)] corrected:

Smoothness

$$\theta_1 x_{,\xi\xi} - 2\kappa_1 x_{,\xi\eta} + \sigma_1 x_{,\eta\eta} = \frac{J_1}{J_3^2}\{(\beta_{,\eta}\chi - \alpha_{,\eta}\mu)x_{,\xi} + (-\beta_{,\xi}\chi + \alpha_{,\xi}\mu)x_{,\eta}\},$$

$$\theta_1 y_{,\xi\xi} - 2\kappa_1 y_{,\xi\eta} + \sigma_1 y_{,\eta\eta} = \frac{J_1}{J_3^2}\{(\beta_{,\eta}\chi - \alpha_{,\eta}\mu)y_{,\xi} + (-\beta_{,\xi}\chi + \alpha_{,\xi}\mu)y_{,\eta}\}.$$

The coefficients in the above equations are given by

$$\chi = \theta_3\alpha_{,\xi\xi} - 2\kappa_3\alpha_{,\xi\eta} + \sigma_3\alpha_{,\eta\eta},$$

$$\mu = \theta_3\beta_{,\xi\xi} - 2\kappa_3\beta_{,\xi\eta} + \sigma_3\beta_{,\eta\eta},$$

where

$$\theta_1 = x_{,\eta}^2 + y_{,\eta}^2 \ , \ \ \kappa_1 = x_{,\xi}x_{,\eta} + y_{,\xi}y_{,\eta} \ , \ \ \sigma_1 = x_{,\xi}^2 + y_{,\xi}^2 \ ,$$

$$\theta_3 = \alpha_{,\eta}^2 + \beta_{,\eta}^2 \ , \ \ \kappa_3 = \alpha_{,\xi}\alpha_{,\eta} + \beta_{,\xi}\beta_{,\eta} \ , \ \ \sigma_3 = \alpha_{,\xi}^2 + \beta_{,\xi}^2 \ .$$

Here, J_1, J_2, and J_3 are the Jacobians of the transformations defined as follows:

$$J_1 = x_{,\xi}y_{,\eta} + x_{,\eta}y_{,\xi} \ , \ \ J_2 = x_{,\alpha}y_{,\beta} + x_{,\beta}y_{,\alpha} \ , \ \ J_3 = \alpha_{,\xi}\beta_{,\eta} + \alpha_{,\eta}\beta_{,\xi} \ .$$

Cell-area distribution

$$\frac{2}{J_3^2}\{b_{v1}x_{,\xi\xi} + b_{v2}x_{,\xi\eta} + b_{v3}x_{,\eta\eta} + a_{v1}y_{,\xi\xi} + a_{v2}y_{,\xi\eta} + a_{v3}y_{,\eta\eta}\} = -J_1^2\frac{\partial}{\partial x}\left(\frac{1}{J_3^2}\right),$$

$$\frac{2}{J_3^2}\{a_{v1}x_{,\xi\xi} + a_{v2}x_{,\xi\eta} + a_{v3}x_{,\eta\eta} + c_{v1}y_{,\xi\xi} + c_{v2}y_{,\xi\eta} + c_{v3}y_{,\eta\eta}\} = -J_1^2\frac{\partial}{\partial y}\left(\frac{1}{J_3^2}\right),$$

where

$$a_{v1} = -x_{,\eta}y_{,\eta} \ , \ \ b_{v1} = y_{,\eta}^2 \ , \ \ c_{v1} = x_{,\eta}^2 \ ,$$

$$a_{v2} = x_{,\xi}y_{,\eta} + x_{,\eta}y_{,\xi} \ , \ \ b_{v2} = -2y_{,\xi}y_{,\eta} \ , \ \ c_{v2} = -2x_{,\xi}x_{,\eta} \ ,$$

$$a_{v3} = -x_{,\xi}y_{,\xi} \ , \ \ b_{v3} = y_{,\xi}^2 \ , \ \ c_{v3} = x_{,\xi}^2.$$

Orthogonality

$$b_{o1}x_{,\xi\xi} + b_{o2}x_{,\xi\eta} + b_{o3}x_{,\eta\eta} + a_{o1}y_{,\xi\xi} + a_{o2}y_{,\xi\eta} + a_{o3}y_{,\eta\eta} = 0,$$

$$a_{o1}x_{,\xi\xi} + a_{o2}x_{,\xi\eta} + a_{o3}x_{,\eta\eta} + c_{o1}y_{,\xi\xi} + c_{o2}y_{,\xi\eta} + c_{o3}y_{,\eta\eta} = 0,$$

where

$$a_{o1} = x_{,\eta}y_{,\eta} \ , \ \ b_{o1} = x_{,\eta}^2 \ , \ \ c_{o1} = y_{,\eta}^2 \ ,$$

$$a_{o2} = x_{,\xi}y_{,\eta} + x_{,\eta}y_{,\xi} \ , \ \ b_{o2} = 2(2x_{,\xi}x_{,\eta} + y_{,\xi}y_{,\eta}) \ , \ \ c_{o2} = 2(2y_{,\xi}y_{,\eta} + x_{,\xi}x_{,\eta}) \ ,$$

$$a_{o3} = x_{,\xi}y_{,\xi} \ , \ \ b_{o3} = x_{,\xi}^2 \ , \ \ c_{o3} = y_{,\xi}^2 \ .$$

In the above equations the *comma* in the subscript denotes partial differentiation with respect to the variable following the comma. The grid equations are linearly combined, discretized by second-order central differencing, and solved iteratively by means of a mixed over-under relaxation technique, with the known grid values from the previous instant of discrete time $x(\xi, \eta; t_{k-1})$, $y(\xi, \eta; t_{k-1})$ taken as the initial guesses. Derivation and details for implementation of this grid generation procedure are given in [19].
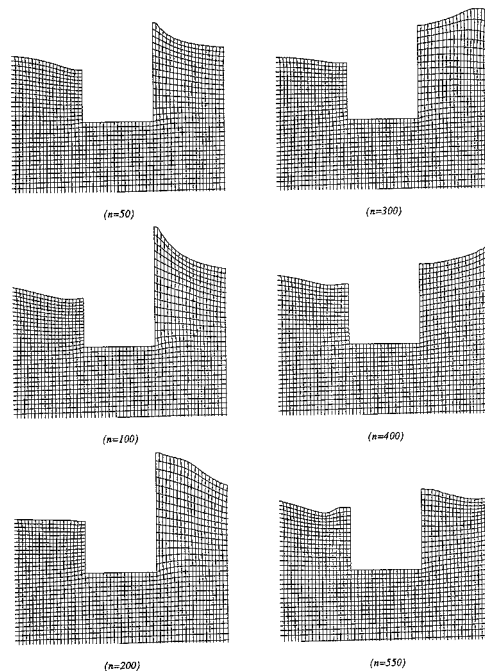
Figure 3. Instantaneous plots of near-field grid system generated for $F_d = 0.5$, $U\delta t/D = 0.005$. n denotes the index of discrete time.

4. Results and discussion

A mesh size of (141×41) is used to obtain the results reported in this paper. The body length and draft are set equal. The length of the physical domain is about thirty body drafts and the depth of the domain is about ten body drafts. Using the reference-space-based grid-generation procedure, we are able to obtain a fine spatial resolution of the zones adjacent to the body boundary and the free surface where flow gradients are expected to be large. At each time step, the free surface and the body boundary are advanced based on the kinematic conditions and the fluid domain discretized by means of the grid equations. Instantaneous near-field plots of the grids generated for a typical nonlinear free-surface case shown in Figure 3 demonstrate the ability of the present grid-generation procedure in adapting to large deformation of the free-surface boundary. An earlier implementation of such a grid method for free-surface wave problem can also be found in [33].

Results presented in this paper correspond to $Re = 10^3$. A nondimensional time-step size $U\delta t/D = 0.005$ was used in all the calculations, which satisfies the numerical stability criterion of the present difference scheme that is applicable to a linear advection-diffusion equation ([34]). The code was partially vectorized, and a typical fully-nonlinear flow case involving 500 time steps required a cpu time of about 30 minutes on a single processor of a Cray-YMP machine.

Accuracy and convergence studies carried out using our algorithm are discussed in [19] and [20]. Such a study was carried out by consideration of a test problem that corresponds to the attenuation of a small-amplitude standing wave due to viscosity. By comparing the nonlinear viscous-flow solutions, obtained with the present algorithm, with those of a linear viscous-flow analysis ([35]) as well as nonlinear inviscid-flow solutions obtained separately

and numerically [19], we established convergency and accuracy of our algorithm with respect to grid refinement (see Figure 4). The findings of this case study also enabled us to determine the appropriate differencing schemes (*e.g.*, upwind differencing for convection term, while central differencing for the diffusion term of the Navier–Stokes equations) to be used in the analysis of the present bow- and stern-flow problem.

4.1. FREE-SLIP AND NO-SLIP 'FREE SURFACES'

In order to understand the mechanisms associated with the generation of upstream trapped vortices, we first consider two simple cases in which the exact nonlinear free-surface conditions are replaced by (i) flat free-slip and (ii) flat no-slip boundary conditions. The boundary conditions corresponding to these flat free-surface cases are given by

(i) Flat free-slip surface:

$$\frac{\partial u}{\partial y} = 0, \ v = 0, \quad \text{and} \quad Y = 0 \quad \text{on } \mathcal{F}. \tag{22}$$

(ii) Flat no-slip surface:

$$u = U, \ v = 0, \quad \text{and} \quad Y = 0 \quad \text{on } \mathcal{F}. \tag{23}$$

Results corresponding to the flat free-slip condition (Equation (22)) are given in Figure 5 in the form of an instantaneous velocity-vector and vorticity-contour plots[1]. We observe the generation of vorticity on the body contour because of the no-slip condition. Negative (clockwise) vorticities generated at the sharp corners of the body merge and form a *macro* vortex trailing the body. Secondary (counter-clockwise) vorticity is generated on the rear face and underside of the body by the primary vorticity as it peels off the sharp leading edge and by the stern macro vortex. Generation of vorticity is not observed on the flat free surface because of the imposed free-slip condition (Equation 22).

Results corresponding to the flat no-slip case, governed by Equation (23), are given in Figure 6. It shows the generation of vorticity on the top boundary, *i.e.*, the no-slip 'free surface'. Strength of the surface vorticity is sufficiently strong to yield a trapped vortex at the junction of the bow and the upstream 'free surface' where the fluid is relatively stagnant (Figure 7a). Similarly, driven by the primary stern vortex, a secondary vortex is generated at the junction of the stern and the 'free surface' (Figure 7b).

It is well known that the generation of vorticity on an actual deformable free surface is relatively weak, compared to that on a no-slip wall surface, and that the jump in vorticity across the free-surface boundary layer is proportional to free-surface curvature (*e.g.* [36], pp. 364–367). At very low Froude number, observations show (or we can formally deduce) that the free-surface deformation is negligibly small compared to the body dimension. Hence, the flat free-slip condition (22) is a valid approximation for the case of a low-speed free-surface flow past a body. The above results thus suggest that there ought to be a different mechanism present that is responsible for the generation of bow vortices as observed in low-speed laboratory experiments.

---

[1] The parameter shown in each of the velocity-vector and vorticity-contour plots is the nondimensional time Ut/D. In all vorticity-contour plots shown in this paper the solid lines denote clockwise vorticity, while the dotted lines denote counter-clockwise vorticity.
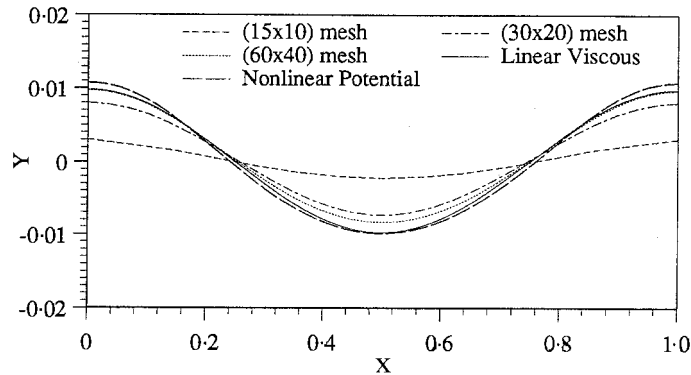
Figure 4. Elevation of a standing wave after one period (500 time steps) corresponding to various grid sizes. Initial wave amplitude $a/\lambda = 0.01$, where λ is the wavelength. The Reynolds number is given by $\lambda(g\lambda)^{1/2}/\nu = 10^4$. Also shown, for comparison purposes, are linear viscous-flow (Lamb [35]) and nonlinear potential-flow results (Ananthakrishnan [19]).

4.2. Free surface with surfactant

In order to determine the effect of surfactants in a low-speed bow flow, we next consider a case in which the free surface ahead of the body is covered with a surfactant. The curve corresponding to $Ut/D = 0$ in Figure 8 shows the initial distribution of the surfactant concentration C ahead of the body. The stern-side free surface is assumed to be clean. The boundary conditions for the bow-side free surface are given by Equation (11), while for the stern-side free surface by Equation (22). We have obtained results for several values of E and R_s, the parameters governing the effect of an insoluble surfactant. The representative case chosen for discussion in this paper corresponds to $E = 0.4$ and $R_s = 10^3$.

Temporal evolution of the surfactant concentration, given in Figure 8, shows that the integral of the concentration over the free surface remains constant in time. This indicates that our solution algorithm conserves mass accurately. The flow ahead of the body reaches a near steady-state after $Ut/D \approx 5.0$. Surfactant concentration and the tangential component of fluid velocity on the free surface (with respect to body-fixed moving frame of reference) at $Ut/D = 6.0$ are given in Figure 9. It shows that the tangential component of velocity practically vanishes underneath the surfactant film. Our results thus confirm that a film of surfactant, trapped at a barrier, could behave as if it were a no-slip membrane.

Instantaneous velocity and vorticity fields corresponding to the above surfactant-covered free-surface case, given in Figure 10, reveal that the flow field resembles that of the no-slip case (Figures 6 and 7) ahead of the body. In particular, we observe that the generation of vorticity underneath the surfactant film, because of nonzero shear, results in the separation of flow upstream of the base body and the formation of a trapped bow vortex (Figure 11). These results thus demonstrate that bow vortices observed in low-speed small-scale model experiments are primarily caused by the presence of surface-active contaminants, not merely by the viscous boundary condition on a clean free surface.

4.3. Generation of bow and stern waves

Results obtained for the case of fully nonlinear free-surface conditions are presented next. Instantaneous velocity and vorticity fields corresponding to $F_d = 0.2$ and zero surface tension
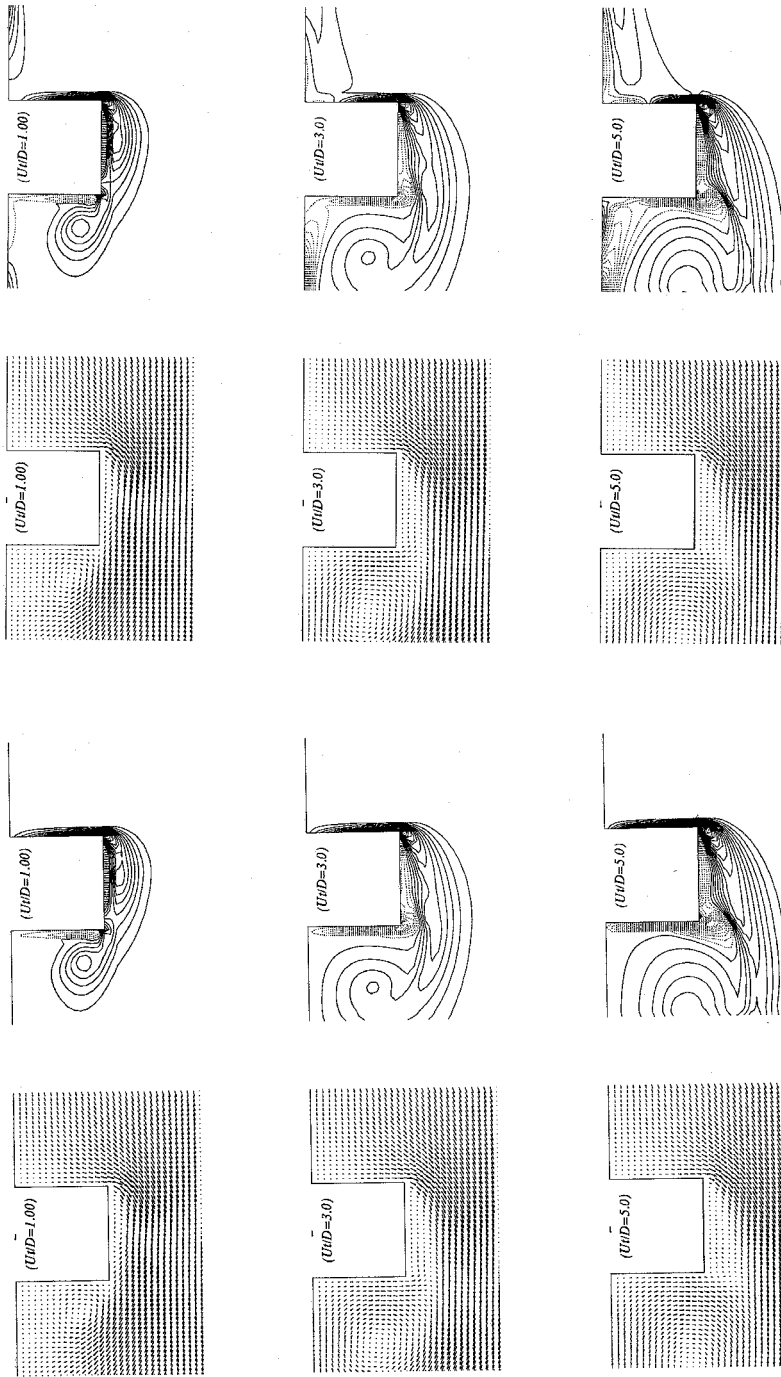
Figure 6. Instantenaeous velocity and vorticity fields corresponding to the case of flat no-slip surface.

Figure 5. Instantenaeous velocity and vorticity fields correponding to the case of flat free-slip surface.
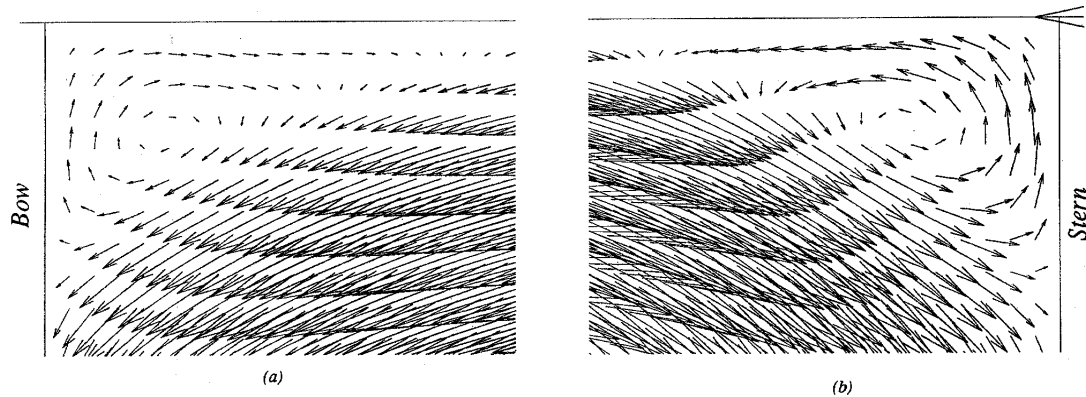
Figure 7. The formation of trapped bow and secondary stern vortices in the case of no-slip surface: nondimensional time $Ut/D = 6$.

(*i.e.*, $We = \infty$) are given in Figures 12 to 14. They show that the flow field well beneath the free surface closely resembles that of the flat free-slip case discussed earlier (Figure 5). In general, the free-surface deformation is small, compared to body draft, because of the small Froude number. A closer observation of the flow ahead of the body reveals the generation of short bow waves propagating upstream (see Figure 14). These figures also show that surface vorticities of alternating signs are being generated by these short bow waves. The surface vorticities remain attached to the free surface as the waves propagate upstream. We do not observe any flow separation ahead of the body at the free surface and, consequently, the inception of bow vortices.

Time evolution of the surface wave profile for $F_d = 0.2$ is shown in Figure 15. Nondimensionalized with respect to U and g, the corresponding time interval is $gt/U = [0, 62.5]$. From this large-time viscous-flow solution, we notice a continuous generation of bow waves of decreasing lengths, as well as the generation of stern waves. The amplitude and slope of the stern waves are quite small because of the low Froude number and also because of the interaction between the free surface and the vortical flow trailing the body. In this context, it is worthwhile to add that the steepness of steady-state potential-flow stern waves trailing a rectangular body at Froude number $F_d = 0.2$ is of the order of only $O(10^{-3})$ ([12]). On the other hand, the short bow waves continue to steepen as they propagate into the stagnant fluid ahead of the body. Generation of such upstream waves are, however, not observed in the case of a translating *submerged* body (see, for *e.g.*, [37] and [38, p. 128]). It is also important to note that these short bow waves are quite different from the classical Cauchy-Poisson waves generated by a translating *pressure system* in which case the transient waves trail the pressure system (see Figure 16). It suggests, therefore, that the generation of short bow waves shown in Figure 15 can be attributed to the interaction of the advancing surface-piercing body with the upstream stagnant fluid. Such continuous generation of short bow waves was first observed in the inviscid-flow results given in [17]. Inviscid-flow results given in [16] show that the generation of bow waves at low Froude number continues even after the stagnation point on the bow reaches the free surface. It is the continuous generation of such short waves that precludes the solution form of bow flow from the possibility of attaining a steady state.
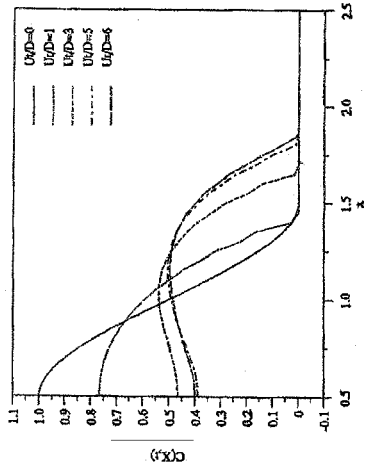
Figure 10. Instantaneous velocity and vorticity fields corresponding to the case of surfactant-covered free surface ahead of the body and free-slip surface behind the body.

Figure 8. Time evolution of surfactant concentration ahead of the body. $x = 0.5$ denotes the bow.
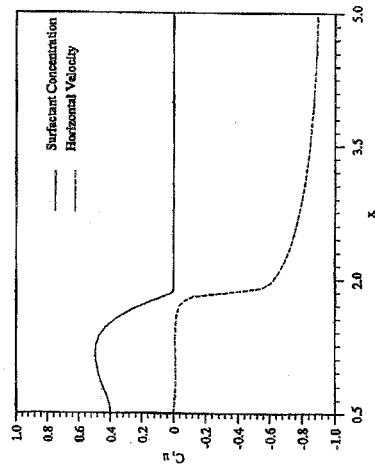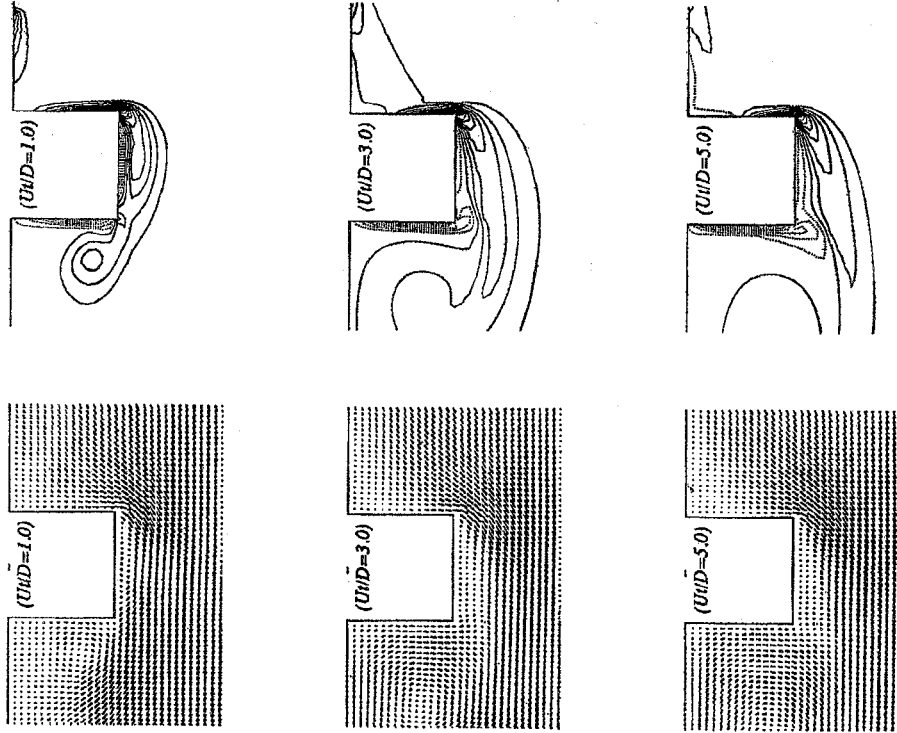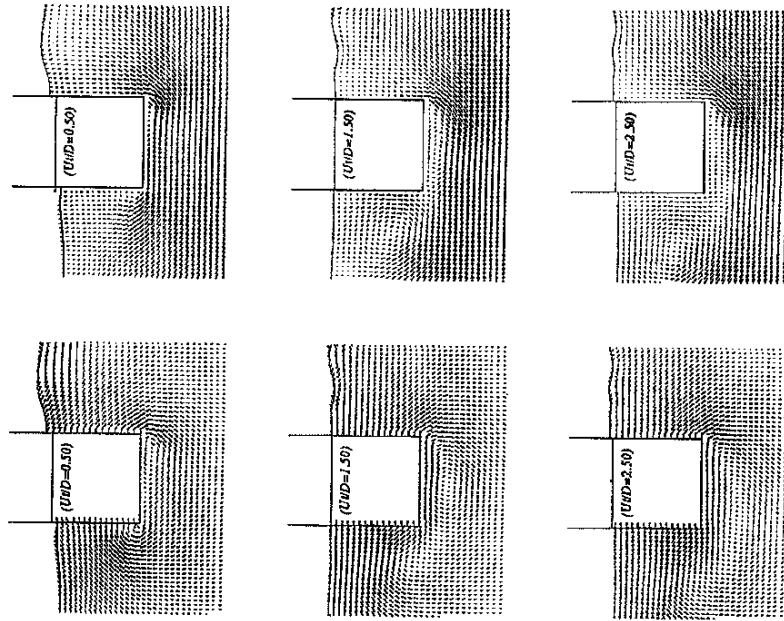

Figure 9. Surfactant concentration and the horizontal velocity component (with respect to moving frame of reference) at $Ut/D = 6$. $x = 0.5$ denotes the bow.

Figure 12. Instantaneous velocity fields, with respect to fixed and moving frames of reference, corresponding to $F_d = 0.2$, $Re = 10^3$, and $We = \infty$. The horizontal line in the body near the free surface denotes the calm water level.
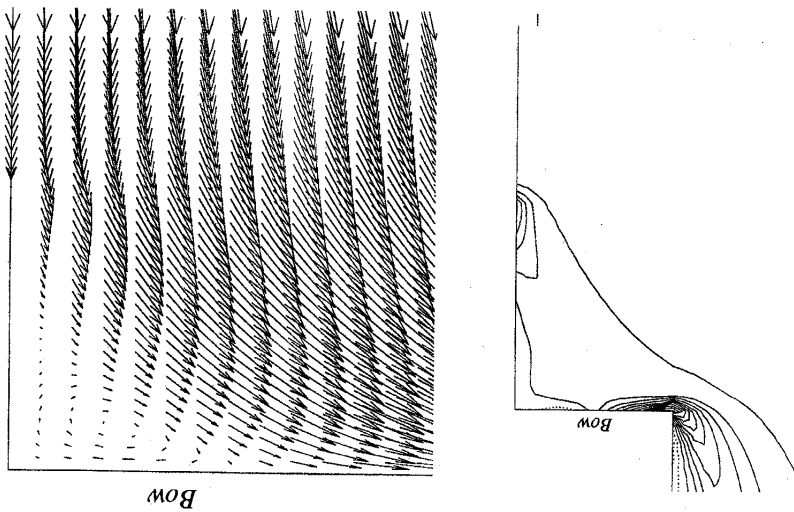
Figure 11. The formation of a trapped bow vortex beneath velocity the surfactant-covered free surface: nondimensional time $Ut/D = 6$.
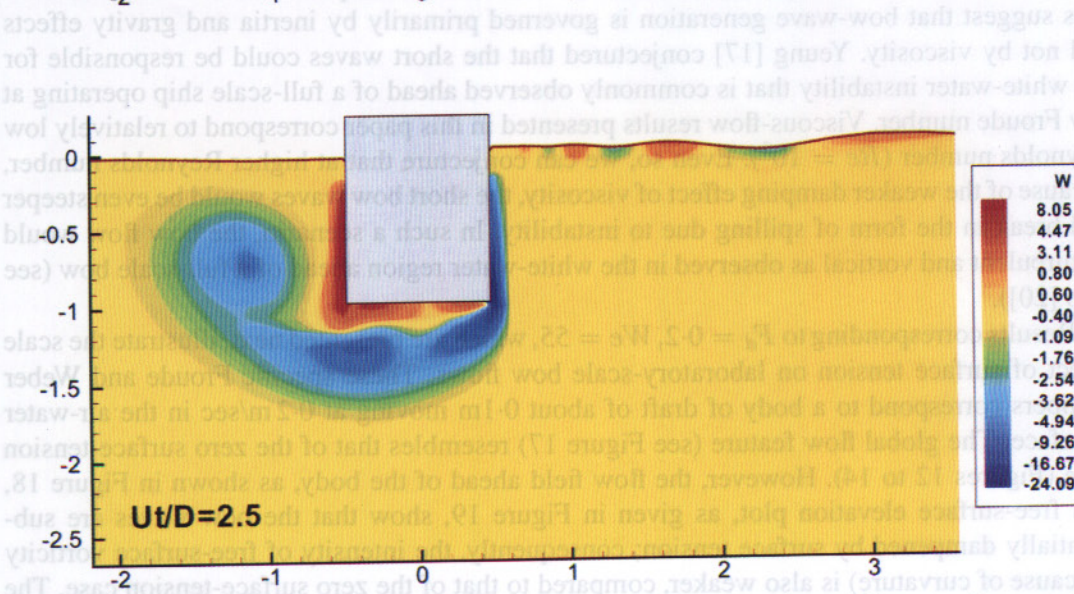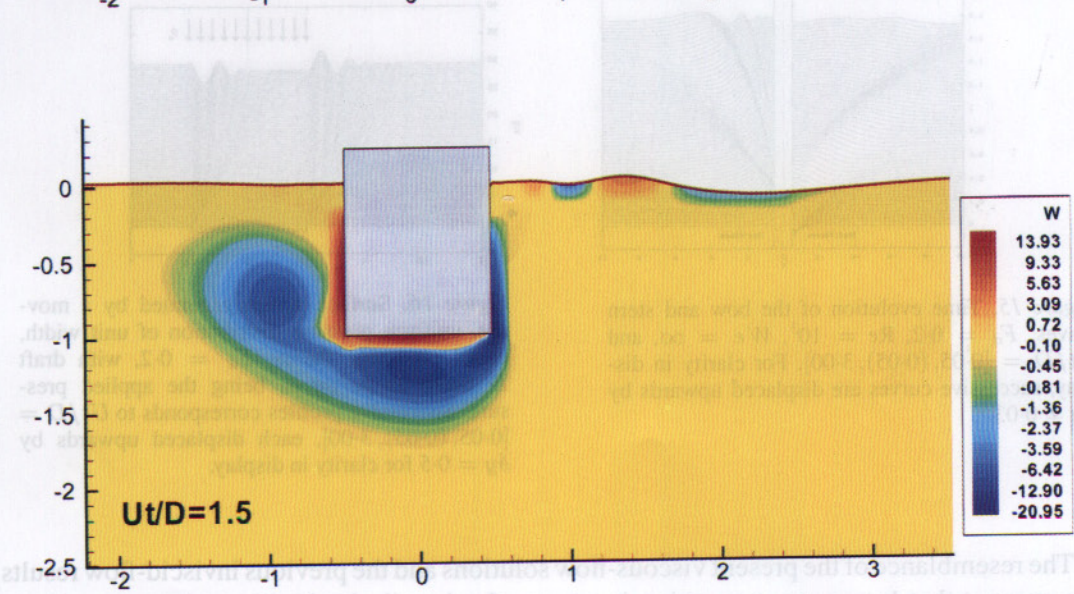
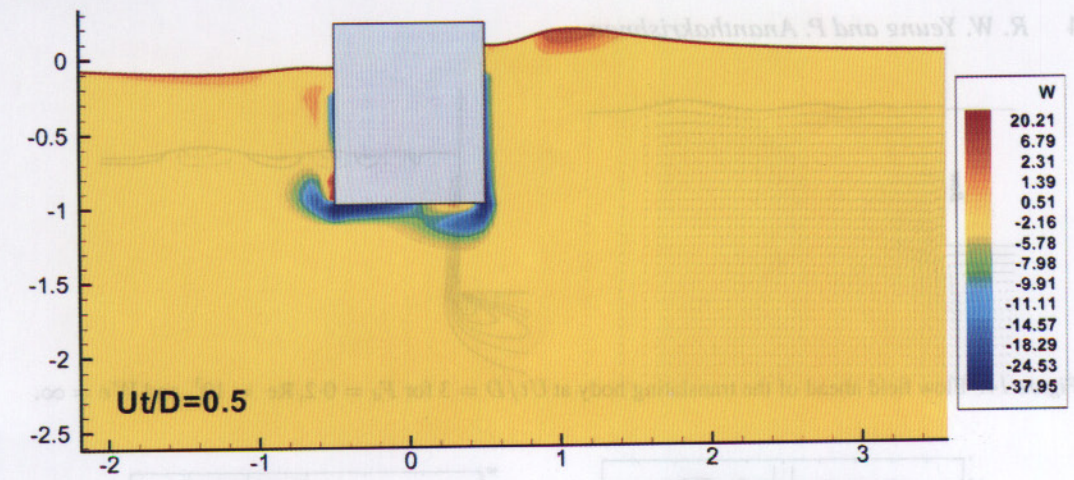*Figure 13.* Instantaneous vorticity fields corresponding to $F_d = 0.2$, Re$= 10^3$, and $We = \infty$. The green-blue spectrum corresponds to clockwise vorticity whereas the orange-red spectrum corresponds to counter-clockwise vorticity.
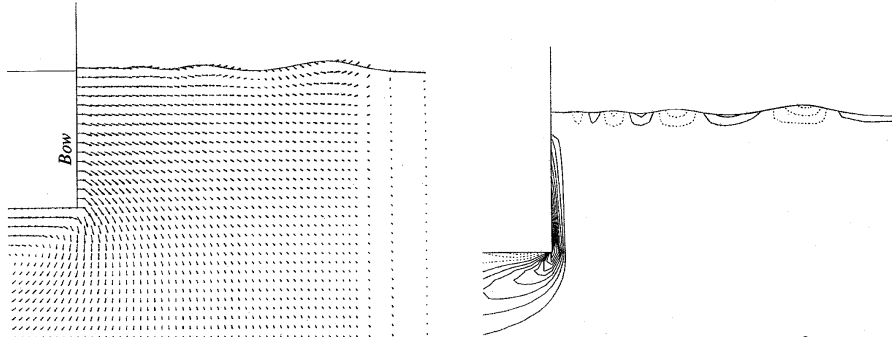
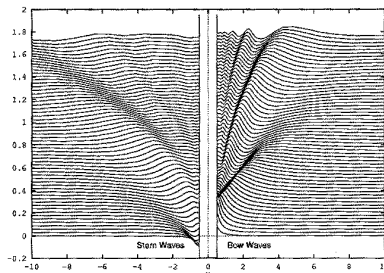*Figure 14.* Flow field ahead of the translating body at $Ut/D = 3$ for $F_d = 0.2$, Re $= 10^3$, and $We = \infty$.

Figure 15. Time evolution of the bow and stern waves: $F_d = 0.2$, Re $= 10^3$, $We = \infty$, and $Ut/D = [0.05, (0.05), 3.00]$. For clarity in display, successive curves are displaced upwards by $\delta y = 0.03$.
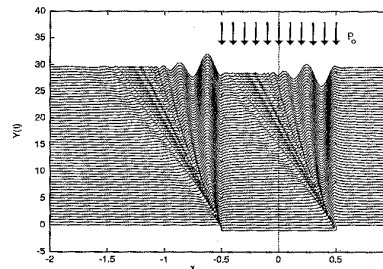

Figure 16. Surface waves generated by a moving, uniform pressure distribution of unit width, based on linear theory. $F_d = 0.2$, with draft D taken as $p_0/\rho g, p_0$ being the applied pressure. Successive profiles corresponds to $Ut/D = [0.05, (0.05), 3.00]$, each displaced upwards by $\delta y = 0.5$ for clarity in display.

The resemblance of the present viscous-flow solutions and the previous inviscid-flow results thus suggest that bow-wave generation is governed primarily by inertia and gravity effects and not by viscosity. Yeung [17] conjectured that the short waves could be responsible for the white-water instability that is commonly observed ahead of a full-scale ship operating at low Froude number. Viscous-flow results presented in this paper correspond to relatively low Reynolds number ($Re = 10^3$). Even so, we can conjecture that at higher Reynolds number, because of the weaker damping effect of viscosity, the short bow waves would be even steeper and break in the form of spilling due to instability. In such a scenario, the bow flow would be turbulent and vortical as observed in the white-water region ahead of a full-scale bow (see also [20]).

Results corresponding to $F_d = 0.2$, $We = 55$, which are presented next, illustrate the scale effect of surface tension on laboratory-scale bow flows. These specific Froude and Weber numbers correspond to a body of draft of about 0.1m moving at 0.2 m/sec in the air-water interface. The global flow feature (see Figure 17) resembles that of the zero surface-tension case (Figures 12 to 14). However, the flow field ahead of the body, as shown in Figure 18, and free-surface elevation plot, as given in Figure 19, show that the bow waves are substantially dampened by surface tension; consequently, the intensity of free-surface vorticity (because of curvature) is also weaker, compared to that of the zero surface-tension case. The wave-dampening effect of surface tension thus explains why spilling-type bow waves, which
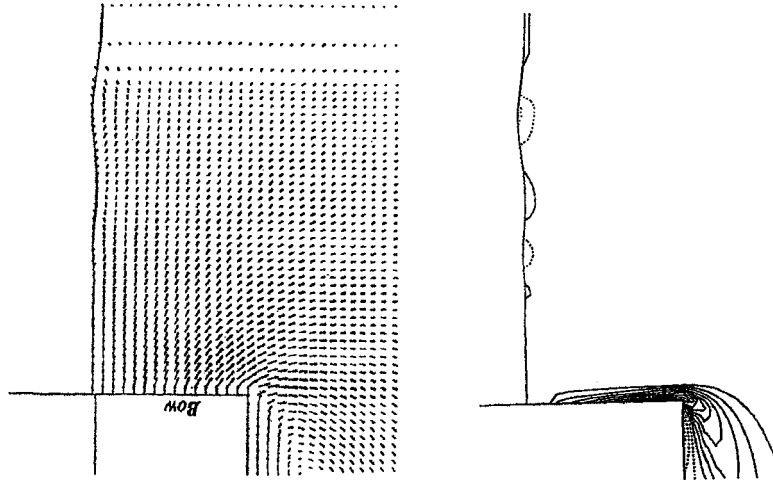
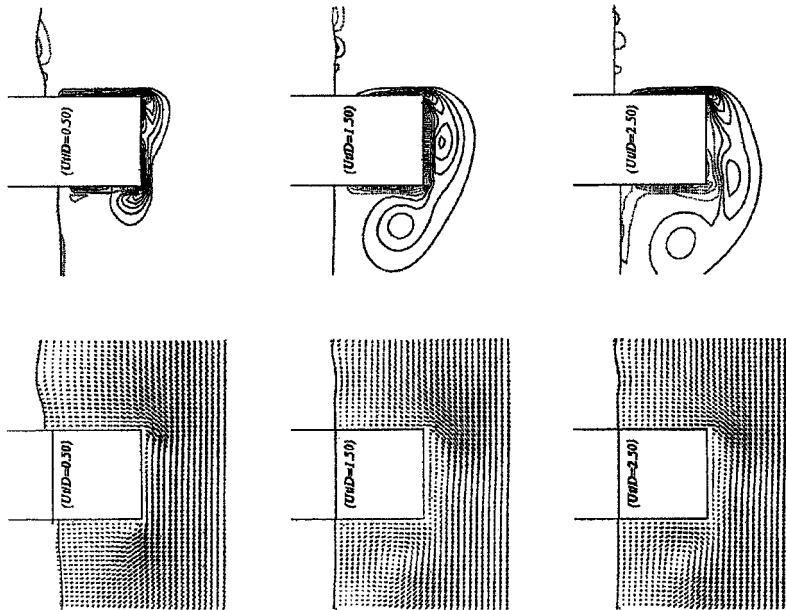*Figure 18.* Flow field ahead of the translating body at $Ut/D = 3$ for $F_d = 0.2$, $Re = 10^3$, and $We = 55$.

Figure 17. Instantaneous velocity (with respect to moving frame of reference) and vorticity fields, for $F_d = 0.2$, $Re = 10^3$, and $We = 55$. The horizontal line in the body near the free surface denotes the calm water level.
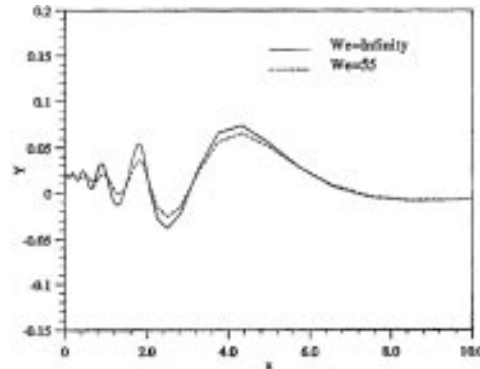
Figure 19. Profiles of bow waves, with and without surface tension, at $Ut/D = 3$. In this graph, bow is at $x = 0$.

constitute white-water at low speed, are not distinctly observed in model-scale experiments (see [10]). The physical origin of stand-alone spilling breakers have recently been studied carefully by Mui and Dommermuth [39] and Duncan *et al.* [40].

Finally, we present results obtained for a large-Froude-number case $F_d = 0.8$. From Figure 20, we observe that an impulsive start of the body generates a splash at the bow that grows unabated initially, thus inhibiting the advancement of the numerical solution in time. Such a consequence of the intersection-point singularity has been encountered in the inviscid bow-flow analysis also [16]. A few remedies have been proposed to overcome this hurdle and to obtain long-time bow-flow solutions ([16], [17]). Here, we follow the approach suggested by Yeung [17], according to which the body is accelerated gently from rest to the steady translational speed as:

$$\frac{u(t)}{U} = \left(\frac{t}{T_s}\right)^3 \left\{6\left(\frac{t}{T_s}\right)^2 - 15\left(\frac{t}{T_s}\right) + 10\right\}, \quad \text{if } t \le T_s,$$

$$= 1, \qquad\qquad\qquad\qquad\qquad \text{if } t > T_s, \qquad (24)$$

where T_s denotes a start-up time. Instantaneous velocity fields corresponding to $F_d = 0.8$ and start-up time $T_s = 2.0$ are shown in Figure 21. The vorticity field at $Ut/D = 2.5$ is shown in Figure 22. We notice that on the rear side of the body, the trailing vortex draws the free surface down from the calm-water level substantially. However, the gentle start allows the fluid to pile up at the bow, which in effect reduces the draft-Froude number. At a later time, the mound of fluid accumulating at the bow overturns and breaks. The upstream stagnation point remains trapped at its initial location beneath the free surface as the bow wave overturns. Such large Froude-number bow-wave phenomena prior to breaking, have already been reported based on the inviscid-flow solutions [16]. Thus, the present large-Froude-number viscous-flow solutions also indicate that the generation of bow waves and the bow-flow character *prior* to wave breaking is governed primarily by inertia and gravity, but not by viscosity.

5. Conclusion

In the present work, we have obtained some new results which can clarify several classic issues related to the bow-flow problem. It is now confirmed that the trapped bow vortex reported in low-speed laboratory-scale experiments is due to the presence of surface-active contaminants and not entirely due to viscosity. Viscous-flow results at low Froude-number
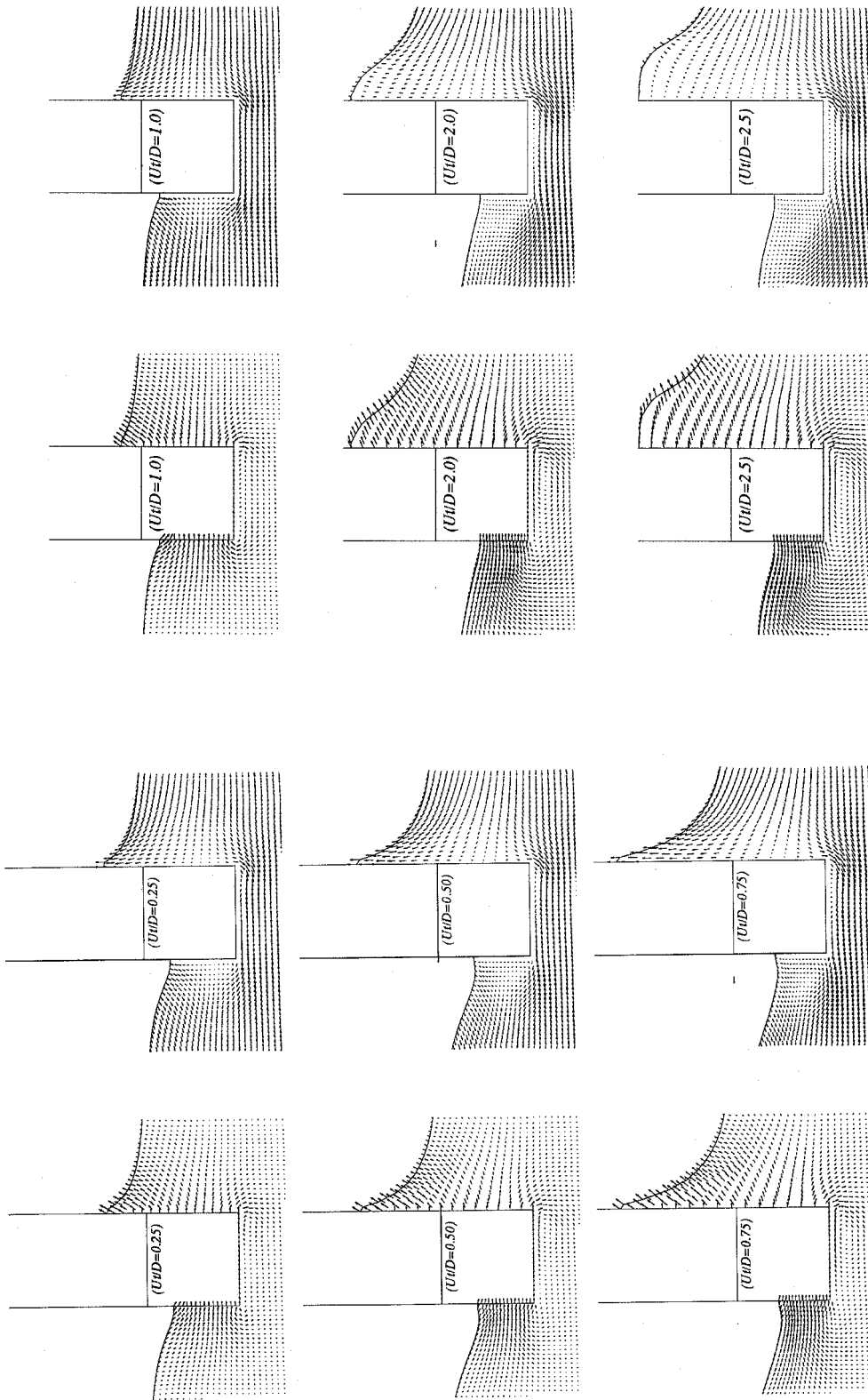
Figure 21. Instantaneous velocity fields, with respect to fixed (left) and moving (right) frames of reference, for $F_d = 0.8$ and $Re = 10^3$ corresponding to a *gentle* start of the body. The horizontal line inside the body denotes the calm water level.

Figure 20. Instantaneous velocity fields, with respect to fixed (left set) and moving (right set) frames of reference, for $F_d = 0.8$ and $Re = 10^3$ corresponding to *impulsive* start of the body. The horizontal line inside the body denotes the calm water level.
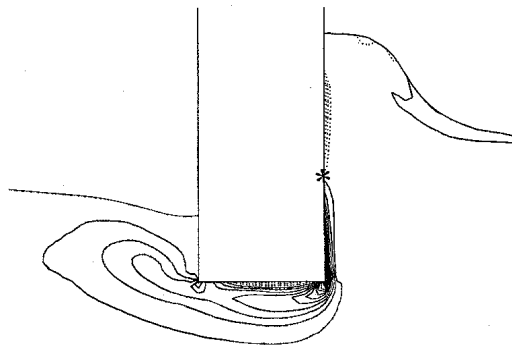
Figure 22. Vorticity field for $F_d = 0 \cdot 8$, Re$= 10^3$, and $T_s = 2$ at $Ut/D = 2 \cdot 5$ corresponding to gentle start of the body. The location of stagnation point on the bow is denoted as '$*$'.

shows a continuous generation of short and steepening bow waves, just as in the inviscid-fluid case [17], which could be the source of white-water bow-wave instability. Surface tension dampens the generation of such short bow waves, the reason why white-water instability is not distinctly observed in a laboratory experiment, in which case the scale effect of surface tension is quite substantial. Viscous-flow results corresponding to large Froude-numbers also resemble those of the inviscid-flow case prior to bow-wave breakings. Our study thus demonstrates that the generation of bow waves and the flow physics ahead of a full-scale ship *prior to any wave breaking* is governed primarily by inertia and gravity and not by viscosity. This finding is contrary to the popular belief that viscosity plays a key role in the bow-wave phenomena, which was based on laboratory observations discussed in the introduction of this paper.

There are however many issues pertaining to bow flows that remain to be tackled or fully resolved. For example, from a scientific viewpoint, solution of the bow-flow problem also necessitates further developments of an accurate model for modeling moving contact lines and for solution methods for analyzing flows after wave breaking. Knowledge of three-dimensional effects and solutions at high Reynolds number are required for a full understanding of the complex bow flow about a practical full-scale ship form. These are objectives of worthy future efforts.

Acknowledgements

References

1. E. Baba, A new component of viscous resistance of ships. *J. Soc. Naval Arch. Japan* 125 (1969) 23–34.
2. K. Suzuki, On the drag of two-dimensional bodies semi-submerged in a surface flow. *J. Soc. Naval Arch. Japan* 137 (1975) 22–35.
3. H. Honji, Observation of a vortex in front of a half-submerged circular cylinder. *J. Phys. Soc. Japan* 40 (1976) 1475–1478.
4. K. Takekuma and K. Eggers, Effect of bow shape on free-surface shear flow. *Proc. Fifteenth Symp. on Naval Hydrodyn.*, Hamburg, Germany (1984) pp. 387–405.

5. Y. Osawa, Aufmessung des Geschwindigkeitsfeldes an und unter der freien Wasseroberfläche in der Bugum-strömung eines stumpfen Körpers. *Bericht 476*, Institut für Schiffbau, Universität der Hamburg, Germany. (in German) (1987) 125 pp.

6. V. C. Patel, L. Landweber, and C. J. Tang, Free-surface boundary layer and the origin of bow vortices. *Report 284*, Iowa Institute of Hydraulic Research, The University of Iowa. (1984) 22 pp.

7. M. A. Grosenbaugh and R. W. Yeung, Flow structure near the bow of a two-dimensional body. *J. Ship Res.* 33 (1989) 269–283.

8. H. J. Lugt, Local flow properties at a viscous free surface. *Phys. Fluids* 30 (1987) 3647–3652.

9. K. Mori, Necklace vortex and bow wave around blunt bodies. *Proc. Fifteenth Symp on Naval Hydrodyn.*, Hamburg, Germany, (1984) pp. 9–20.

10. H. Maruo and M. Ikehata, Some discussions on the free-surface flow around the bow. *Proc. Sixteenth Symp. on Naval Hydrodyn.* Berkeley, California (1986) pp. 65–77.

11. G. Dagan and M. P. Tulin, Two-dimensional free-surface gravity flow past blunt bodies. *J. Fluid Mech.* 51 (1972) 529–543.

12. J.-M. Vanden-Broeck and E. O. Tuck, Computation of near-bow and stern flows using series expansion in the Froude number. *Proc. Second Int. Conf. Num. Ship Hydrodyn.* Berkeley, California, (1977) pp. 377–387.

13. E. O. Tuck and J.-M. Vanden-Broeck, Splashless bow flows in two dimensions? *Fifteenth Symp. on Naval Hydrodyn.* Hamburg, Germany (1984) pp. 293–301.

14. M. A. D. Madurasinghe, Splashless ship bows with stagnant attachment. *J. Ship Res.* 32 (1988) 194–202.

15. E. O. Tuck, Ship-hydrodynamic free-surface problems without waves. *J. Ship Res.* 35 (1991) 277–287.

16. M. A. Grosenbaugh and R. W. Yeung, Nonlinear free-surface flow at a two-dimensional bow. *J. Fluid Mech.* 209 (1989) 57–75.

17. R. W. Yeung, Nonlinear bow and stern waves – inviscid and viscous solutions. In: T. Miloh (ed.) *Mathematical Approaches in Hydrodynamics*, Philadelphia: Society of Industrial and Applied Mathematics (1991) pp. 349–369.

18. H. Miyata, Finite-difference simulation of breaking waves. *J. Comp. Phys.* 65 (1986) 179–214.

19. P. Ananthakrishnan, *Surface waves generated by a translating two-dimensional body: effects of viscosity.* Ph.D. dissertation, Dept. Naval Arch. and Offshore Eng., University of California at Berkeley (1991) 155 pp.

20. R. W. Yeung and P. Ananthakrishnan, Vortical flows with and without a surface-piercing body. *Proc. Nine-teenth Symp. on Naval Hydrodyn.* Seoul, S. Korea, (1992) pp. 212–238.

21. J. V. Wehausen and E. V. Laitone, Surface Waves. In: S. Flügge (ed.) Handbuch der Physik ix. Berlin: Springer-Verlag (1960) pp. 447–778.

22. V. G. Levich, *Physicochemical Hydrodynamics.* Englewood Cliffs: Prentice-Hall Inc, (1962) 700 pp.

23. H. W. Hoogstraten, H. C. J. Hoefsloot, and L. P. B. M. Janssen, Marangoni convection in V-shaped containers. *J. Eng. Math.* 26 (1992) 21–37.

24. E. B. Dussan V. and S. H. Davis, On the motion of a fluid-fluid interface along a solid surface. *J. Fluid Mech.* 74 (1974) 71–95.

25. É. É Marcovich, Effect of surface tension on the free outflow of a wetting fluid from a horizontal tube. *Fluid Dyn.* 23 (1988) 230–237.

26. J. Koplik, J. R. Banavar, and J. F. Willemsen, Molecular dynamics of fluid flow at solid surfaces. *Phys. Fluids*, A5, (1989) 781–794.

27. E. B. Dussan V., The moving contact line: the slip boundary condition. *J. Fluid Mech.* 77 (1976) 665–684.

28. C. Huh and S. G. Mason, The steady movement of a liquid meniscus in a capillary tube. *J. Phy. Soc. Japan* 81 (1977) 401–419.

29. R. W. Yeung and P. Ananthakrishnan, Oscillation of a floating body in a viscous fluid. *J. Eng. Math.* 26 (1992) 211–230.

30. A. J. Chorin, Numerical solution of incompressible flow problems. *Studies in Num. Anal.* 2 (1968) 64–71.

31. A. J. Chorin, Numerical solution of the Navier–Stokes equations. *Math. Comp.* 22 (1968) 745–762.

32. J. Kim and P. Moin, Application of a fractional-step method to incompressible Navier–Stokes equations. *J. Comp. Phys.* 59 (1985) 308–323.

33. R. W. Yeung and M. Vaidhyanathan, Non-linear interaction of water waves with submerged obstacles. *Int. J. Num. Meth. Fluids* 14 (1992) 1111–1130.

34. C. Hirsch, *Numerical Computation of Internal and External Flows: vol. 1 Fundamentals of Numerical Discretization.* Wiley (1988) 515 pp.

35. H. Lamb, *Hydrodynamics.* New York: Dover (1932) 738 pp.

36. G. K. Batchelor, *An Introduction to Fluid Mechanics.* Cambridge: Cambridge University Press (1967) 615 pp.

37. Y. J. Kim and J. H. Hwang, Two dimensional transient motions with large amplitude by time domain method. *Proc. Sixteenth Symp. on Naval Hydrodyn.* Berkeley, California (1986) pp. 415–426.

38. M. Vaidhyanathan, *Separated flows near a free surface*. Ph.D. dissertation, Dept. Naval Arch. and Offshore Eng. University of California at Berkeley (1993) 197 pp.
39. R. C. Y. Mui and D. G. Dommermuth, The vortical structure of parasitic capillary waves. *J. Fluids Eng.* 117 (1995) 355–361.
40. J. H. Duncan, V. Philomin, M. Behres, and J. Kimmel, The formation of spilling breaking waves. *Phys. Fluids* 6 (1994) 2558–2560.